Marangoni instability triggered by selective evaporation of a binary liquid inside a Hele-Shaw cell

Ricardo Arturo Lopez de la Cruz[1], Christian Diddens[1,2], Xuehua Zhang[3,1], and Detlef Lohse[1,4]

[1]Physics of Fluids Group, Max-Planck-Center Twente for Complex Fluid Dynamics, Mesa+ Institute, and J. M. Burgers Centre for Fluid Dynamics, Faculty of Science and Technology, University of Twente, P.O. Box 217, 7500 AE Enschede, The Netherlands

[2]Department of Mechanical Engineering, Eindhoven University of Technology, P.O. Box 513, 5600 MB Eindhoven, The Netherlands

[3]Department of Chemical and Materials Engineering, University of Alberta, Edmonton, Alberta, T6G 1H9, Canada

[4]Max Planck Institute for Dynamics and Self-Organization, Am Faßberg 17, 37077 Göttingen, Germany

1. Extended setup and humidity/temperature time series

In figure 1 we show in more detail the position of the chip, the dry and humid nitrogen inlets, and the humidity and temperature sensor. The gas flow was not directed to the chip, but to the side. The plastic wrapping was not hermetically sealed, therefore the gas was able to escape from different places around the gas phase volume (see figure 1(a) and (c)). Notice that the gas phase is not confined by the Hele-Shaw cell. Instead the gas phase is a large three-dimensional volume. Because the ethanol vapor is denser than air, it can sink away from the edge of the chip. However, we do not have a quantification of this effect.

Four examples of the relative humidity time series are shown in figure 2(a). Two of them correspond to experiments with rhodamine 6G (R6G) and two for μPIV experiments. For each pair, we show examples with the flow on and off. For the latter, the relative humidity was inside the desired range throughout the experiment. In the realization shown with R6G, the humid flow was on every time the relative humidity was below 49%. In the μPIV example, the dry flow was on every time the relative humidity was above 50%. We adjusted the thresholds at which the flow was active to keep the average value close to 50%. The flow rates were in the range of 1 ± 0.1 L/min.

The corresponding temperatures are shown in figure 2(b). As can be seen, in three cases the temperature increased about half a degree over 15 min, because of the heating of the electronics. Therefore, the temperature for a new experiment was higher than in the previous case.

Figures 2b and 4d from the main text, and figure 4 in this document, include the realizations corresponding to the conditions in figure 2. The impact of the variations of the conditions inside the chamber seem to be relatively small. However, the lifetime of the instability could be affected by such variations.

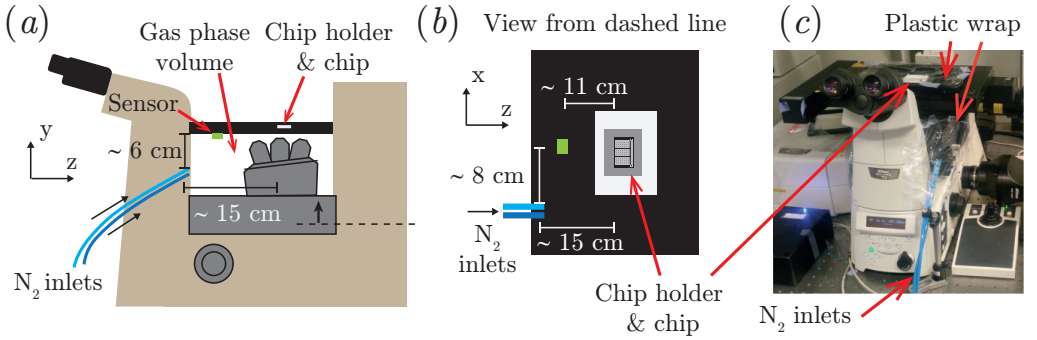

FIGURE 1. Disposition of chip, nitrogen inlets and sensors. (*a*) Sketch of the side view of the confocal microscope, showing the inlets of dry and humid nitrogen (N_2) and their location with respect to the chip. The humidity and temperature sensor (green rectangle) is placed inside the gas volume, approximately at the same height as the chip. (*b*) View from the horizontal dashed line drawn in (*a*). The distances between the inlets, sensor and chip are shown. (*c*) Photograph showing the actual setup to show the wrapping around the microscope. Gas was able to escape from small spaces all around the microscope.

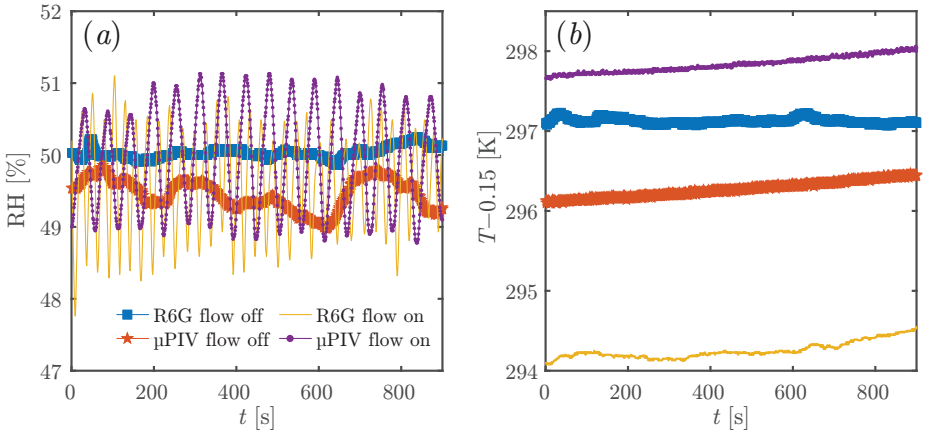

FIGURE 2. Examples of the (*a*) relative humidity (RH) and (*b*) temperature over a period of 900 s for two experiments with rhodamine 6G and two μPIV experiments. For each kind of experiment we show cases where the flow was on or off. The temperature changes during each experiment because of the heating caused by the electronics. The majority of our experiments are between 296 and 298 K.

2. Contact angle inside the chip

In order to get an estimate of the contact angle, we took volumetric scans of the meniscus formed at the back channel of the chip. We adjusted the flow so the meniscus would stay in place during the scan. In figure 3(*a*) we show an example of one of the horizontal planes. The inset shows a zoom to the back channel of the chip. A red square indicates the approximate position where the scan was taken. The distance between planes was of 1.1 or 2 µm for different repetitions.

By taking a slice along the x^{d} direction we could obtain the vertical profile of the meniscus as shown in figure 3(*b*). The left side of the picture shows the data obtained from the fluorescent channel while the right side shows data obtained from the reflection channel. From the reflection data we get the location of the walls. In figure 3(*c*) we

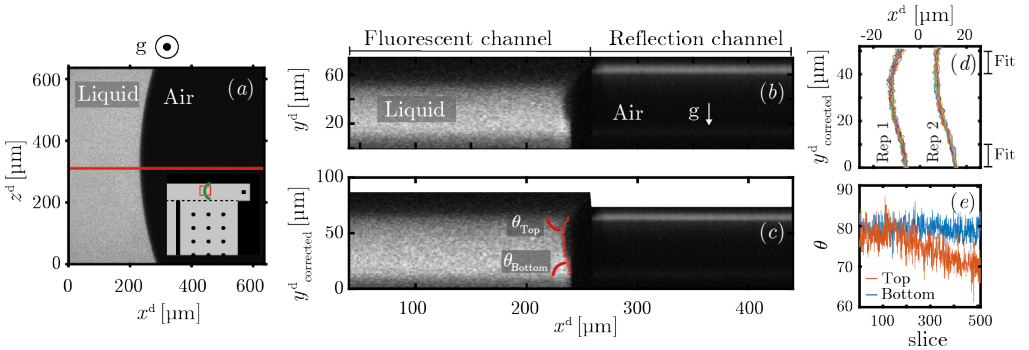

FIGURE 3. Example of contact angle measurement. (*a*) Horizontal slice showing the interface between air and the ethanol-water mixture dyed with rhodamine 6G. The image was taken at the back channel. *Inset*: Sketch showing a portion of the chip. The red square gives and indication of the measurement location and the green curved line represents the meniscus. (*b*) Reconstructed slice (normal to the walls of the chip) taken at the horizontal red line marked in (*a*). We have mixed the image obtained from the fluorescent channel (left half) and the reflection channel (right half). (*c*) Same as in (*b*) but the liquid side has been corrected for the different refractive index (1.36). The red dots indicate the interface. (*d*) Vertical profile of the meniscus at different slices. Two different repetitions at 2 different locations in the back channel are shown. The contact angle was obtained by making linear fits in the ranges marked. (*e*) The contact angle measured at each slice (different z^{d} locations) for repetition 1.

show the same image but the liquid side (fluorescent channel) has been corrected for the different refractive index inside the mixture (1.36 (Scott Jr 1946)).

To find the interface we made use of the fact that the intensity at a given y^{d} position behaves closely to a step function. The intensity is approximately constant with respect to x^{d} before and after the step. We determined the mean intensity before the step, I_0, and after the step, I_1. The location of the interface was assumed to be where the intensity was given by $0.5 * (I_0 + I_1)$. The red dots in figure 3(c) show the corresponding found interface.

In figure 3(d) we show a few meniscus profiles obtained at different vertical slices of the same repetition (Rep 1). The horizontal position of each profile was translated horizontally by subtracting the mean x^{d} position to show the profiles on top of each other. A second set of vertical profiles taken at a different location inside the chip is shown for comparison (Rep 2).

The contact angle was finally obtained by fitting a line to the data in a range of 10 µm as indicated in figure 3(d). The resulting angles for all the slices are shown in figure 3(e) for repetition 1. The results from 3 different measurements are shown in table 1.

From these contact angles we can have an estimation of the pressure drop across the meniscus at the evaporating edge in the Hele-Shaw cell, by considering a meniscus between parallel plates and two different contact angles, $\Delta p^{\mathrm{d}} = \gamma(\cos\theta_{\mathrm{Bottom}} + \cos\theta_{\mathrm{Top}})/\delta^{\mathrm{d}}$. This implies that the pressure drop is between 10^2 and 10^3 Pa.

3. Estimation of pressure drop inside the chip

In order to keep the chip filled, we kept a continuous flow from the inlet of the chip. This flow requires an over-pressure at the inlet of the chip. In order to have an estimate of the pressure drop from the back channel to the open edge we have assumed a perfectly rectangular channel with dimensions $w^{\mathrm{d}} = 1$ cm and $\delta^{\mathrm{d}} = 20$ µm, meaning that the aspect ratio is given by $\delta^{\mathrm{d}}/w^{\mathrm{d}} = 0.002$. This small aspect ratio allowed us to make use

	θ_{Bottom}	θ_{Top}
Rep 1	79 ± 2	75 ± 4
Rep 2	78 ± 3	89 ± 5
Rep 3	76 ± 3	86 ± 4

TABLE 1. Average contact angle and standard deviations for 3 repetitions. Repetitions 2 and 3 are two consecutive measurements at the same location but different from the location of repetition 1.

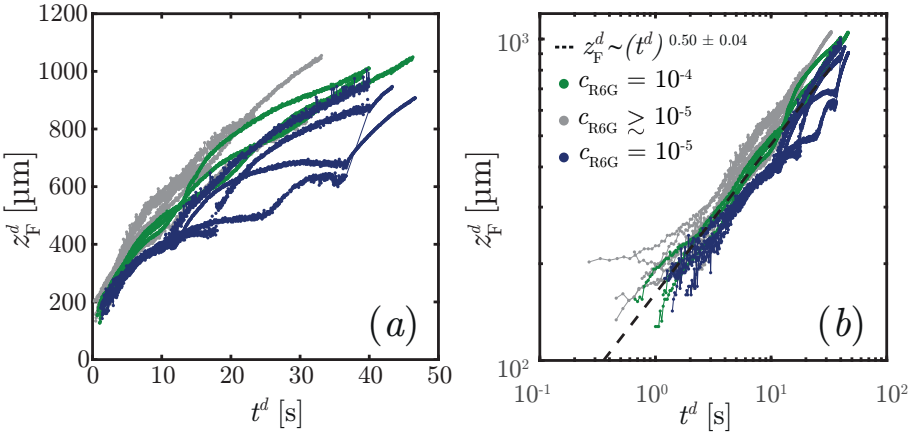

FIGURE 4. Height z_F^d over time for different mass fractions of rhodamine 6G with (a) linear and (b) logarithmic scales.

of the limiting equation for the pressure drop (Bruus 2008) :

$$\Delta p^{\mathrm{d}} = \frac{12\mu_0^{\mathrm{d}} L^{\mathrm{d}} Q^{\mathrm{d}}}{w^{\mathrm{d}}(\delta^{\mathrm{d}})^3(1 - 0.63\frac{\delta^{\mathrm{d}}}{w^{\mathrm{d}}})}, \tag{3.1}$$

where Δp^{d} is the pressure drop along the channel, $\mu_0^{\mathrm{d}} = 2.5$ mPa s is the viscosity of the fluid, $L^{\mathrm{d}} = 1.8$ cm is the length of the channel, and $Q^{\mathrm{d}} = 2.8 \times 10^{-12}$ m^3 s^{-1} is the volumetric flow. Then, the pressure drop is $\Delta p^{\mathrm{d}} = 19$ Pa. Therefore, the pressure caused by the replenishing flow is very small compared with the pressure drop at the meniscus, calculated in the previous section. Deformations of the interface due to this pressure are hence not expected.

4. Rhodamine 6G concentration effects

Figure 4(b) shows measurements of z_F^{d} for two different rhodamine 6G concentrations, namely 10^{-4} (0.1 g/L) and 10^{-5} (0.01 g/L). The variation for a fixed concentration (blue curves), specially after 7 s, are larger than those caused by changing the concentration. The large variations are caused, in part, by the non-sharp boundary between the arches and the bulk. Over time this boundary becomes even more diffuse, thus the position of the summit is not as easy to track. The time at which merging takes place can also affect the value of z_F^{d}, given that the growth is faster just after merging. This is evidenced by the sudden jumps in z_F^{d}. Therefore, if a merging event takes place at different times for different experiments, z_F^{d} will be different.

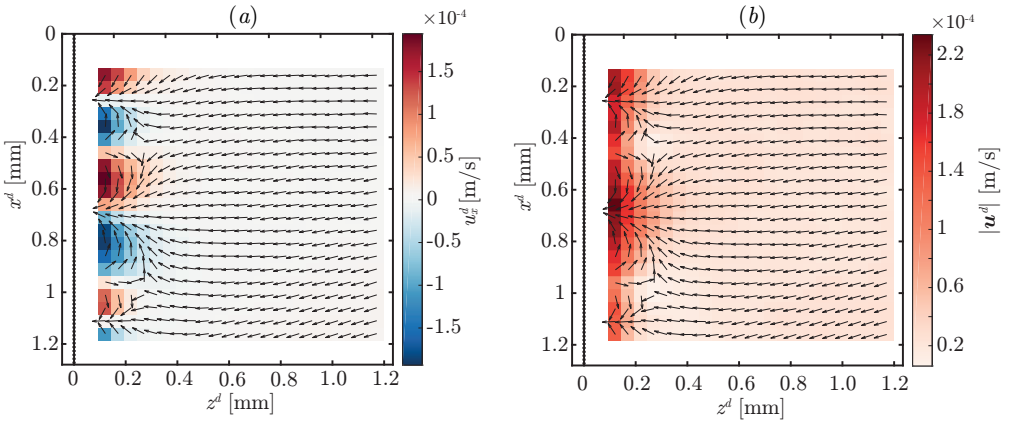

FIGURE 5. (*a*) Vertical component of the velocity and (*b*) the total velocity magnitude corresponding to the same case as in figure 4(*b*) in the main text. The size of the arrows was kept constant to highlight the direction.

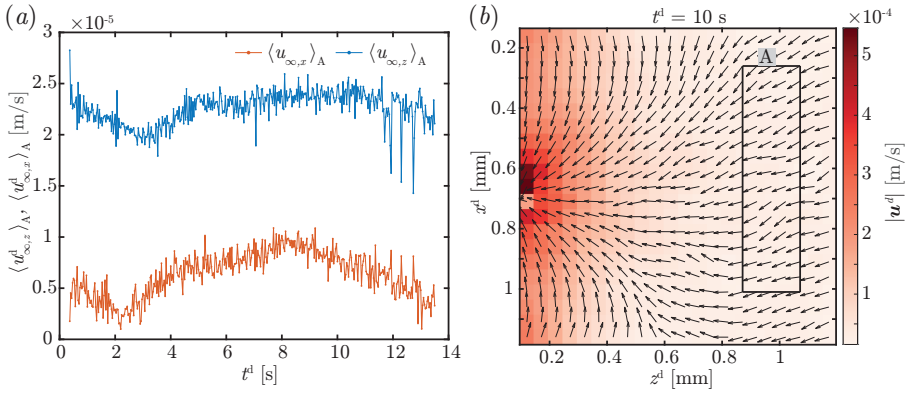

FIGURE 6. (*a*) Time series of the velocity far away from the edge. The values shown were obtained as a spatial average over the area A marked by the rectangle in (*b*). (*b*) Velocity field obtained from a single frame at $t = 10$ s. The size of the arrows was kept constant to highlight the direction.

Despite this larger variability, the match of z_F^d between experiments and simulations is reasonably good given that simulations were performed up to 10 s. Furthermore, as shown by figure 4(*b*), the overall trend for z_F^d stays close to a square root dependence with time besides the accelerated growth during the merging events.

5. Further observations from μPIV

5.1. *Vertical component and magnitude of velocity*

Here we show the vertical component (figure 5(*a*)) and the magnitude (figure 5(*b*)) of the velocity corresponding to the field shown in figure 4(*b*) in the main text. The black dotted vertical line indicates the position of the edge of the chip.

5.2. *Evaporation velocity*

During the first 10 seconds over which we compared experiments with simulations, the velocity away from the edge stays approximately constant as shown by figure 6(*a*). The

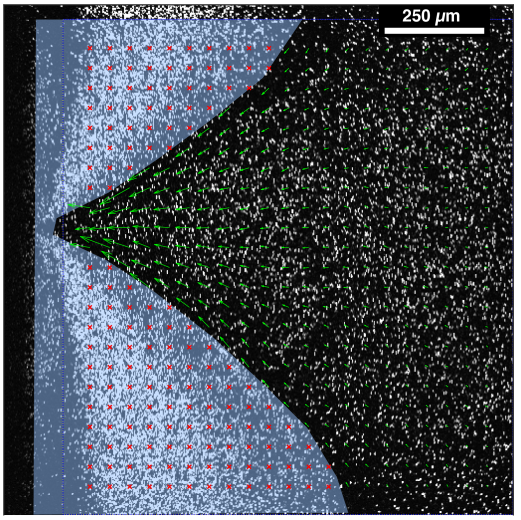

FIGURE 7. Example of a frame used to obtain the velocity field around 100s. The blue region was masked.

velocities shown were obtained as a spatial average taken over the area enclosed by the black rectangle plotted in figure 6(b), where we also show the velocity field at 10 s. At longer times, we expect the evaporation rate to reduce as the gradient of ethanol reduces. Once the instability is vanishing, the velocity caused by evaporation reduces to about 10 μm/s.

5.3. *Mask used for μPIV at 100s*

Figure 7 shows an example of a frame used in μPIV. The blue region is the mask used to avoid taking measurements inside the Marangoni rolls once the density of particles was too high. This was the case for the yellow curves in figure 4(d) in the main text. At the moment shown in figure 7 it might seem that the mask is larger than needed, however later the high density region extends to occupy the masked region.

6. Values of $\overline{E}$ and Ma_s^* obtained from simulations

In table 2 we show the corresponding time limits and the values of $\overline{E}$ and Ma_s^* for each simulation used to obtain figure 10 of the main text.

7. Simulation meshes and domain size

We used three different kinds of mesh configurations for the different simulations we performed. Examples of the meshes are shown in figure 8 with definitions of different length scales needed to determine the mesh. The numerical values of these length scales are shown in table 3. The simulation numbers corresponds with those shown in table 2.

Mesh 1 was used for the large size simulation presented in section 3.3 of the main text. These kind of meshes consisted of triangular elements with a higher density close to the interface, where a higher resolution is needed. The number of elements reduces with distance from the interface. This is the kind of mesh that was used for the gas domain in all simulations. While setting up the simulations, we determined the size at the gas-liquid interface Δx^i, at the far edge in the liquid $\Delta x^{\mathrm{l},\infty}$, and at the far edge in

#	$t_{\mathrm{fit},1}$	$t_{\mathrm{fit},2}$	$\overline{E}$	$\mathrm{Ma}_{\mathrm{s}}^{*}$
1	6.85×10^{2}	1.37×10^{3}	1.56×10^{-3}	6.33×10^{2}
2	1.71×10^{3}	2.40×10^{3}	1.73×10^{-3}	7.03×10^{2}
3	1.03×10^{3}	1.71×10^{3}	1.63×10^{-3}	6.64×10^{2}
4	2.05×10^{3}	2.74×10^{3}	1.75×10^{-3}	7.13×10^{2}
5	1.37×10^{3}	2.05×10^{3}	1.74×10^{-3}	7.08×10^{2}
6	1.71×10^{3}	2.40×10^{3}	1.74×10^{-3}	7.09×10^{2}
7	2.40×10^{3}	3.42×10^{3}	1.76×10^{-3}	7.16×10^{2}
8	2.40×10^{3}	3.42×10^{3}	1.76×10^{-3}	7.16×10^{2}
9	2.05×10^{2}	4.11×10^{2}	6.87×10^{-3}	2.79×10^{3}
10	2.05×10^{2}	4.11×10^{2}	6.87×10^{-3}	2.79×10^{3}
11	2.05×10^{2}	4.11×10^{2}	6.88×10^{-3}	2.79×10^{3}
12	3.42×10^{2}	4.79×10^{2}	6.91×10^{-3}	2.81×10^{3}
13	1.37×10^{2}	2.74×10^{2}	6.68×10^{-3}	2.71×10^{3}
14	1.37×10^{2}	2.74×10^{2}	6.70×10^{-3}	2.72×10^{3}
15	2.05×10^{2}	3.42×10^{2}	6.56×10^{-3}	2.66×10^{3}
16	2.05×10^{2}	4.11×10^{2}	6.96×10^{-3}	2.83×10^{3}
17	6.85×10^{1}	1.37×10^{2}	1.68×10^{-2}	6.82×10^{3}
18	2.74×10^{1}	6.85×10^{1}	1.71×10^{-2}	6.94×10^{3}
19	4.11×10^{1}	9.59×10^{1}	1.58×10^{-2}	6.40×10^{3}
20	3.42×10^{1}	6.85×10^{1}	1.68×10^{-2}	6.82×10^{3}
21	5.48×10^{1}	1.37×10^{2}	1.51×10^{-2}	6.12×10^{3}
22	3.42×10^{1}	6.85×10^{1}	1.64×10^{-2}	6.65×10^{3}
23	1.23×10^{2}	1.92×10^{2}	1.73×10^{-2}	7.05×10^{3}
24	3.42	6.85	2.35×10^{-1}	9.56×10^{4}
25	3.42	6.85	2.43×10^{-1}	9.86×10^{4}
26	3.42	6.85	2.29×10^{-1}	9.31×10^{4}
27	3.42	6.85	2.31×10^{-1}	9.40×10^{4}
28	3.42	6.85	2.44×10^{-1}	9.91×10^{4}
29	3.42	6.85	2.33×10^{-1}	9.46×10^{4}
30	3.42	6.85	2.33×10^{-1}	9.46×10^{4}
31	3.42	6.85	2.15×10^{-1}	8.73×10^{4}
32	3.42	6.85	2.33×10^{-1}	9.47×10^{4}
33	3.42	6.85	2.24×10^{-1}	9.10×10^{4}
34	3.42	6.85	2.42×10^{-1}	9.81×10^{4}
35	3.42	6.85	2.22×10^{-1}	9.00×10^{4}
36	3.42	6.85	2.41×10^{-1}	9.81×10^{4}
37	3.42	6.85	2.01×10^{-1}	8.16×10^{4}
38	3.42	6.85	2.28×10^{-1}	9.25×10^{4}
39	3.42	5.82	3.79×10^{-1}	1.54×10^{5}
40	3.42	6.85	3.81×10^{-1}	1.55×10^{5}
41	3.42	5.48	3.69×10^{-1}	1.50×10^{5}
42	3.42	6.85	3.89×10^{-1}	1.58×10^{5}

TABLE 2. Time limits $t_{\mathrm{fit},1}$ and $t_{\mathrm{fit},2}$ over which the values of the mass fraction gradient $\overline{E}$, and the growth rate σ were calculated. The corresponding values of $\overline{E}$ and the modified Marangoni number $\mathrm{Ma}_{\mathrm{s}}^{*}$ (calculated using $\overline{E}$) are shown too.

the gas $\Delta x^{\mathrm{g},\infty}$ (see figure 8 for a graphical definitions of these quantities). These length scales determine the resolution. The corresponding values are shown in table 3.

Mesh 2 included a layer on the liquid side where the triangular elements where arranged to create a rectangular mesh (see second and third columns of figure 8). This layer extended from the interface up to a distance L_{BL}, then the mesh would behave as Mesh 1, with the number of elements decreasing the further away from the interface.

Mesh 3 was divided in three stages: first the rectangular layer up to L_{BL} (as in Mesh 2), then a section of increasing element size over a distance L_{BL2} (as in Mesh 1) and finally a section of coarser resolution. In this last section a blending factor was used to determine if the element size would be homogeneous and given by the size of $\Delta x^{\mathrm{l},\infty}$ (blending factor equal to 1), or if the resolution would linearly increase up to $\Delta x^{\mathrm{l},\infty}$ (blending factor smaller than 1). This would then affect how fast the resolution would decrease over the distance L_{BL2}.

8. Mismatch of boundary condition

As mentioned in the main text, for the simulation used for comparison with experimental results, we reduced the resolution in order to avoid exceedingly long simulation times. This came at the cost of a mismatch of the boundary condition between fluxes, meaning that

$$\rho D \partial_z c_{\mathrm{e}} \neq (1 - c_{\mathrm{e}}) j_{\mathrm{e}} - c_{\mathrm{e}} j_{\mathrm{w}} \,. \tag{8.1}$$

In figure 9 we show both the left and the right hand sides of equation (8.1). In figure 9(a) both quantities are shown as function of the coordinate x at $t = 1.37 \times 10^4$. In figure 9(b) we show the same quantities over time, but this time averaged along the x coordinate. The gradient in mass fraction that is imposed by the flux in the gas, cannot be captured properly by the low resolution used in the liquid side. In fact, no matter how small the resolution is chosen, it is not possible to perfectly satisfy (8.1), the convection-diffusion equation and the conservation of mass on the linear shape functions used for the composition space. Hence, this type of error needs to be accepted, i.e. the mass is conserved at the expense of not perfectly reproducing the imposed normal composition gradient due to preferential evaporation directly at the interface. Nevertheless, since for this simulation we are more interested on the phenomena that takes place in the bulk, this mismatch does not seem to represent a big problem at distances larger than the concentration boundary layer.

On the other side, the kinematic boundary condition (equation 3.10 in the main text) is properly captured despite the low resolution. Furthermore, by comparing with simulations with a smaller simulation domain and higher resolutions, we confirmed that the values of the velocity in the z direction at the interface $u_z(z = 0)$ reached the same order of magnitude as in the larger simulation. Therefore, the velocity field should only be affected weakly by the mismatch. This explains why there is a good comparison with experiments. However, we can not expect that the exact values of mass fraction observed in simulations represent those in experiments. It can then be questioned how the growth of the front agreed with experiments. We consider that this suggests that it is the velocity field, by means of the size of the Marangoni rolls, which determines the penetration depth z_{F}. Since we only look at the position z where the mass fraction reaches the far field value, it is not as important how much ethanol has been lost. Instead, what is more important is up to which position has the ethanol-poor solution been advected back into the bulk by the Marangoni rolls.

#	L^{g}	L^{l}	W	$\Delta x^{\mathrm{g},\infty}$	$\Delta x^{\mathrm{l},\infty}$	Δx^{i}	Mesh kind[a]	L_{BL}	L_{BL2}	Blending factor	BC[b]
1	500	12.5	17.5	17.5	1.75	0.175	1	-	-	-	P
2	500	12.5	20	20	1	0.05	1	-	-	-	P
3	500	12.5	25	25	2.5	0.125	1	-	-	-	P
4	500	12.5	17.5	17.5	1.75	0.175	2	1.05	-	-	P
5	500	25	25	25	2.5	0.25	2	0.5	-	-	NP
6	500	37.5	50	50	25	0.25	2	0.5	-	-	NP
7	500	12.5	20	20	1	0.05	3	0.75	4	1	P
8	500	12.5	20	20	1	0.05	3	0.75	8	0.5	P
9	125	5	10	10	0.5	0.025	1	-	-	-	P
10	125	5	10	10	0.5	0.025	1	-	-	-	NP
11	125	10	10	10	0.5	0.025	1	-	-	-	P
12	125	15	10	10	0.5	0.025	1	-	-	-	P
13	125	5	15	15	0.75	0.0375	1	-	-	-	P
14	125	15	15	15	0.75	0.0375	1	-	-	-	P
15	125	2.5	10	10	0.5	0.05	2	1	-	-	P
16	125	5	10	10	0.5	0.025	3	0.5	2	1	P
17	5	1	5	5	0.25	0.025	1	-	-	-	P
18	5	5	5	5	0.25	0.0125	1	-	-	-	P
19	5	1	7.5	7.5	0.375	0.0375	1	-	-	-	P
20	5	7.5	7.5	7.5	0.375	0.01875	1	-	-	-	P
21	5	1	10	10	0.5	0.05	1	-	-	-	NP
22	5	7.5	10	10	0.5	0.025	1	-	-	-	NP
23	5	5	5	5	0.25	0.0125	3	0.05	1	1	P
24	3.5	0.5	2	0.4	0.08	0.008	1	-	-	-	P
25	3.5	0.5	2	0.5	0.1	0.005	1	-	-	-	P
26	3.5	0.5	2	0.5	0.1	0.01	1	-	-	-	P
27	3.5	1.5	2	0.5	0.1	0.01	1	-	-	-	P
28	3.5	2	2	2	0.1	0.005	1	-	-	-	P
29	3.5	2	2	0.5	0.1	0.01	1	-	-	-	P
30	3.5	2.5	2	0.5	0.1	0.01	1	-	-	-	P
31	3.5	0.5	3	0.75	0.15	0.015	1	-	-	-	NP
32	3.5	0.5	3.5	3.5	0.0875	0.00875	1	-	-	-	P
33	3.5	0.5	5	5	0.125	0.0125	1	-	-	-	P
34	3.5	0.5	2	2	0.1	0.01	2	0.025	-	-	P
35	3.5	0.5	2	2	0.1	0.01	2	0.014	-	-	P
36	3.5	0.5	2	2	0.1	0.02	2	0.025	-	-	P
37	3.5	2	2	0.5	0.1	0.005	3	0.1	0.8	0.5	P
38	3.5	2	2	2	0.1	0.01	3	0.1	0.4	0.5	P
39	2.25	1	2	1	0.1	0.005	1	-	-	-	P
40	2.25	2	2	1	0.1	0.005	1	-	-	-	P
41	2.25	2	3	1.5	0.15	0.0075	1	-	-	-	P
42	2.25	2	2	1	0.1	0.005	3	0.1	0.8	1	P
43	2.25	60	60	60	6	0.6	1	-	-	-	P

TABLE 3. Domain characteristics of the simulations used for linear stability comparison. Quantities are normalized using the chip height $\delta^{\mathrm{d}} = 20$ µm. Simulation #43 corresponds to the case shown in figure 6 in the main text.

[b] Kind of boundary condition, either periodic (P) or non periodic (NP).

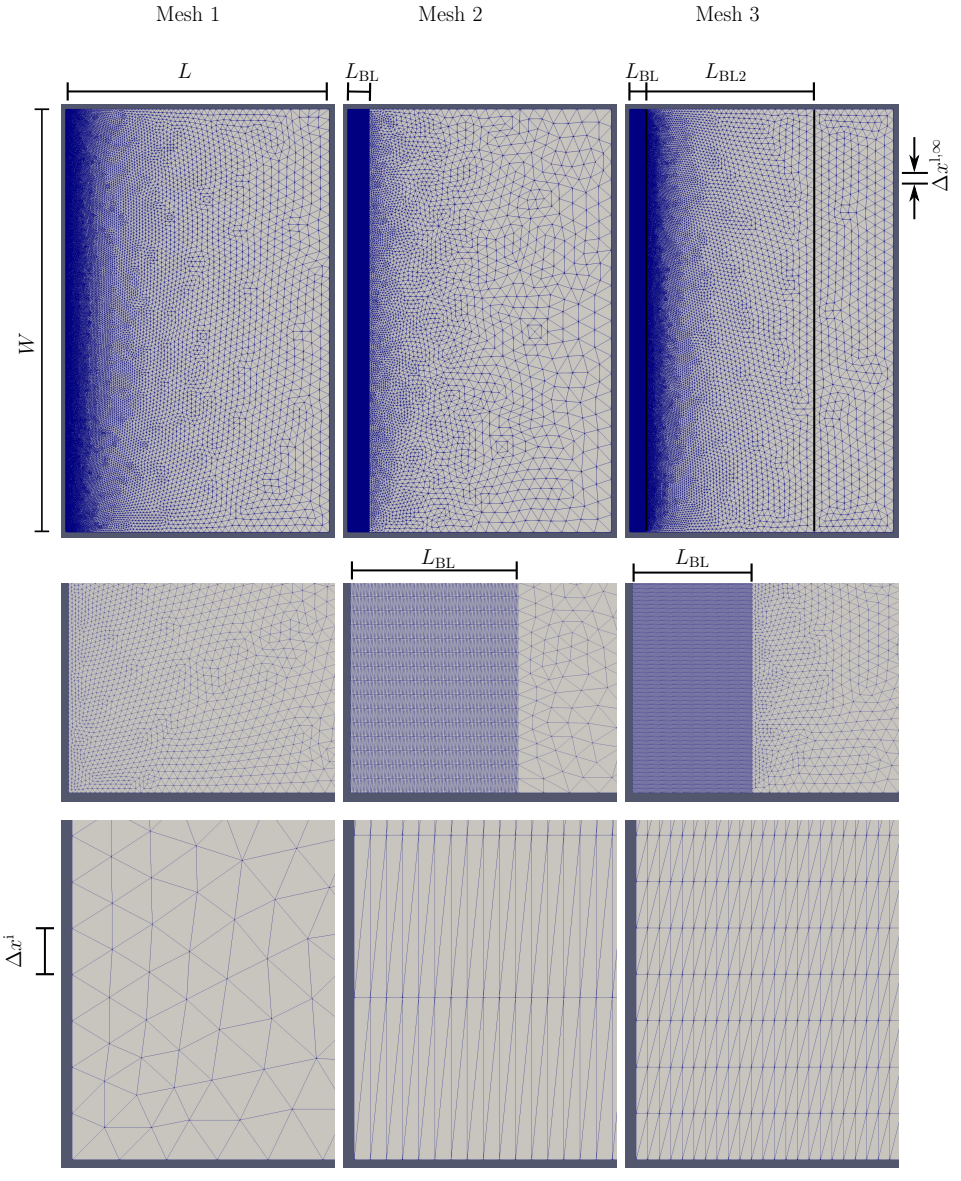

FIGURE 8. Examples of the three kind of meshes used in the liquid phase for comparison with linear stability analysis. For each case, we show two levels of zoom of the lower left corner. We also marked the definitions of the different distances reported in table 3. In the case of the gas phase we only used meshes of kind 1, but mirrored horizontally. The left edge corresponds to the gas-liquid interface.

9. Velocity comparison between simulations and experiments

Here we discuss in more detail the comparison of the velocity between experiments and simulations. In figure 10(a) we show velocity profiles $\langle |u| \rangle_x$ as function of z for four different times. The solid lines correspond to simulations and the crosses to experiments.

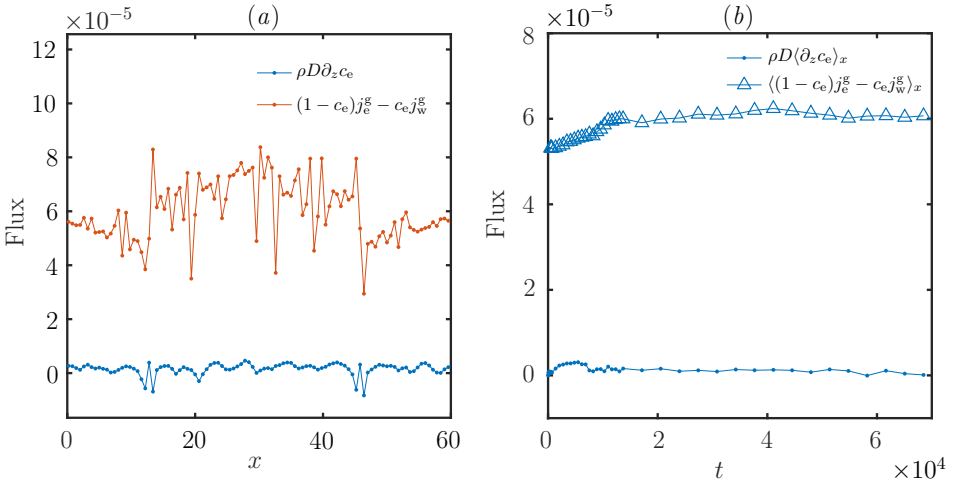

FIGURE 9. Example of the mismatch between the left and right hand side in the boundary condition given by equation (3.12) in the main text. (a) Fluxes along the interface at $t = 1.37 \times 10^4$. (b) Average fluxes over time.

If we take $t_1 = 6.85 \times 10^3$, then the other times correspond to $t_2 = 3t_1$, $t_3 = 7t_1$, and $t_4 = 9t_1$. In the case of experiments, the the first three velocity profiles have a strong change, while the last profile is very similar to the third one. In simulations, there is a strong change from the first profile to the second, and from the third to the fourth profile, while the second and third profiles are quite similar. These changes are easier to see from figure 10(b) where we show the evolution of the averaged velocity at fixed z positions. It is clear, that the velocity evolves in a staggered manner with three steps visible in both experiments and in simulations. Therefore, we can expect that if we look at velocity profiles that correspond to the same step in figure 10(b), they will be very similar, while if we look at velocity profiles at different steps, then they will look quite different.

Figures 10(c) and (d) show snapshots of the experiment and simulation respectively (in experiments we averaged 31 frames to make it easier to see the arches). Two merging events took place over time, reducing the number of arches to one, both in experiment and in simulation. However, the merging events took place at different moments in time. By comparing the times on the snapshots with the times at which the velocity has changed into a new step, we can see that a new step corresponds with a merging event. During the time between merging events the velocity stays approximately constant, therefore, as we already mentioned, if we look back at the profiles from figure 10(a), they do not change very strongly until a merging event takes place.

When we compare experiments and simulations, we can see that although the simulation has a slightly smaller velocity, as long as both have gone trough the same number of merging events, the profiles coincide quite well. Furthermore, in both cases, the distance where the velocity reaches the far-end value coincides quite well as can be seen from figure 10(a).

One reason for the mismatch between the times for merging comes from our uncertainty in the initial time in experiments. However, the time zero uncertainty should not affect the duration between merging events, which is not the same between experiments and

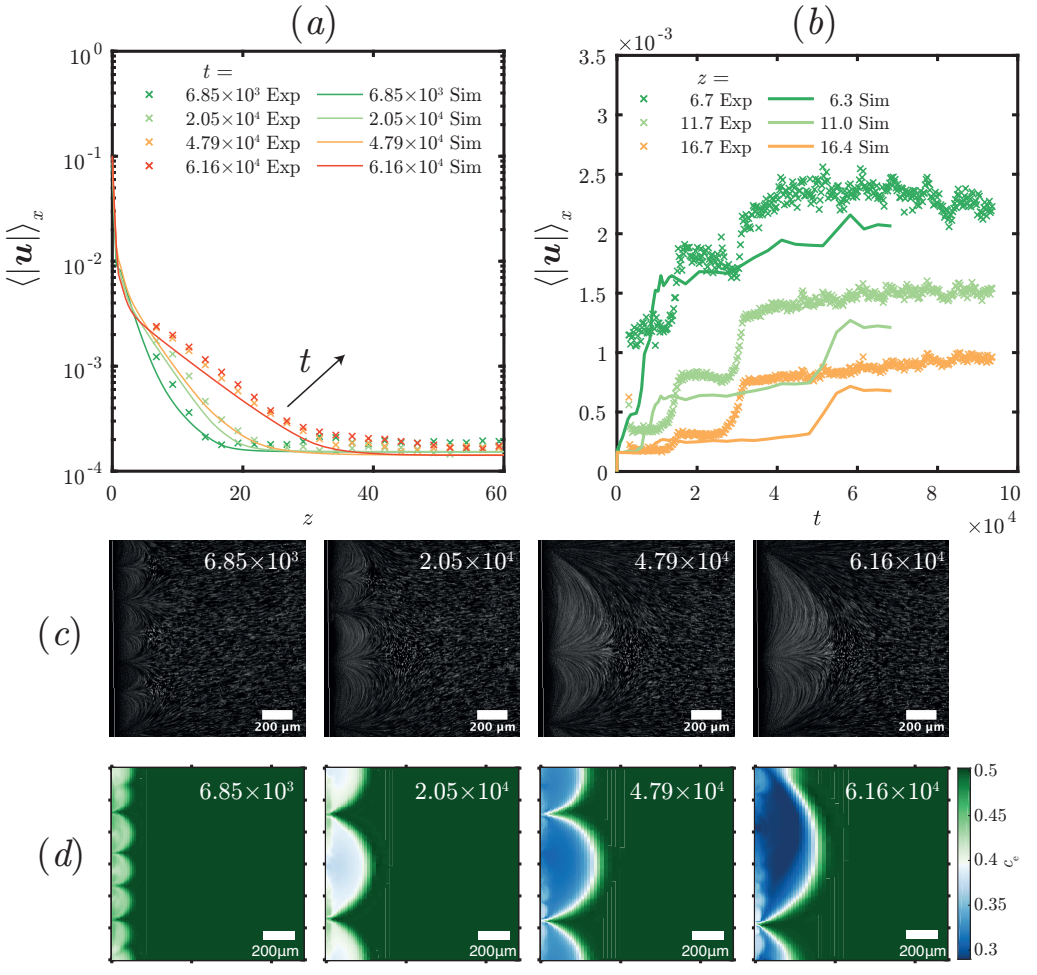

FIGURE 10. Velocity comparison between experiments and simulations at different times and positions. (a) Average velocity profiles at four different times obtained from simulation and from experiments. The profiles correspond to a single frame, while in the main text the profiles where obtained from velocity fields which were already an average over 31 frames. (b) Average velocity as a function of time at three different distances from the edge. Since the resolutions are not the same between experiments and simulations, we took the closest positions for comparison. (c) Evolution of the instability obtained from experiments seeded with particles. Each image was obtained as an average over 31 frames centered at the indicated time. The times correspond to those shown in (a). The white vertical lines in each panel, indicate the position of the edge of the chip. (d) Mass fraction fields obtained from simulations for the corresponding times.

simulation. This could come from irregularities at the edge of our chip, which are not present in simulations. However, further investigation is needed to determine what initiates a merging event.

The steps in the velocity in figure 10b, suggest that as long as the arches have a similar size, the velocity field should be approximately the same. In figure 11 we compare velocity measurements both from experiments and simulations at multiple positions, times, and realizations for arches with a similar size.

The velocity fields u_z in figure 11(a)-(b) correspond to the same realization but at two different times, while no merging event has taken place (second step in figure 10(b)). We

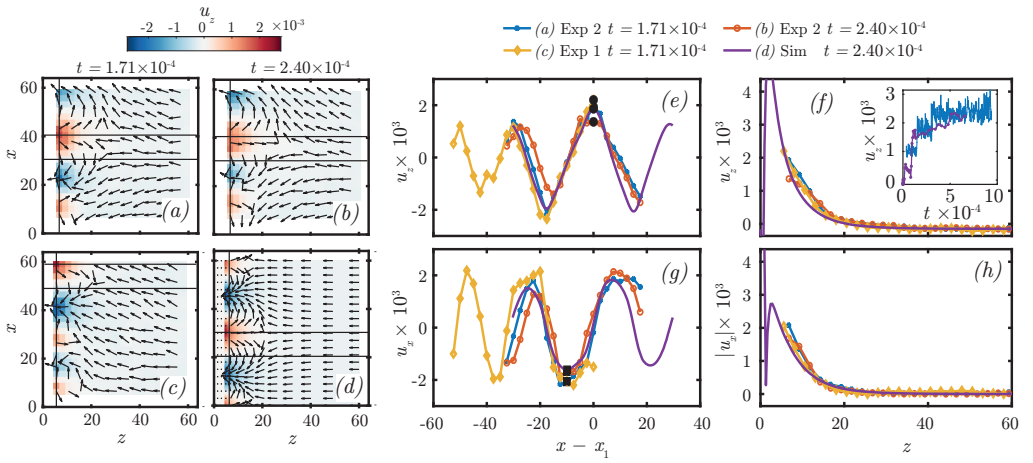

FIGURE 11. Velocity field comparison for similar sized arches. (*a*-*b*) Velocity fields for a single realization at two different times without merging taking place. (*c*) Velocity field of a different realization at the same time as in panel (*a*) where an arch of similar half-size is visible at the top–left corner. (*d*) Velocity field obtained from simulations at the same time as in panel (*b*) with the central arch about the same size as in panels (*a*) and (*b*). Velocity profiles were taken at the place marked by the solid vertical black lines. Panel (*e*) shows u_z and panel (*g*) shows u_x. The profiles where displaced to align the centers of the arches. Velocity profiles along z are shown in panels (*f*) and (*h*). They were taken at positions marked with solid horizontal black lines on top of the velocity fields and correspond to the maxima and minima marked with black circles and squares in panels (*e*) and (*g*). *Inset*: Time series of u_z obtained at the center of single arches. The blue curve is from experiments and the purple heavier line is from simulations. The arches tracked are such that they were one of the parents merging into the following arch.

will focus on the larger arch of about 40 length units in the x direction. In figure 11(*c*) a different realization is shown at the same time as in figure 11(*a*) where an arch of half-width of 20 length units is visible. Finally, figure 11(*d*) shows a velocity field obtained from simulations at the same time as in figure 11(*b*) where the central arch is also close to 40 unit lengths. In the later plot we have made the velocity equal to zero in the region where we cannot measure in experiments, otherwise the much larger velocity close to the edge would make it difficult to make a comparison with experiments.

From each of the four velocity fields, we have taken a profile at approximately the same z position, namely $z = 6.75, 6.75, 5.56, 6.29$ corresponding to fields (*a*)-(*d*) (this positions are marked with vertical black lines). Figures 11(*e*) and (*g*) show the profiles for both u_z and u_x. The x coordinate was shifted such that the maximum in u_z is placed at $x - x_1 = 0$, allowing us to compare the velocity of the large arch. The comparison is reasonably good, indicating that for a given arch size, the velocity is approximately the same despite the time, or the realization. Furthermore, the velocity from the simulations agrees quite well.

Profiles along z are also plotted in figure 11(*f*) and (*h*) at the x positions marked in figure 11(*e*), and (*g*) with black circles and black squares. This indicates that if at a single time the arches visible are of approximately the same size, the averaged velocity profiles should give approximately the same information as compared to profiles at a single position.

Finally, the inset of figure 11(*f*) shows the time series of $u_z(t)$ obtained at the center of a single arch and $z = 6.75$. The arches that we tracked can be seen in figure 10(*c*). In the first two snapshots we measured the velocity at the center of the lowest arch. In the last

two snapshots we followed the only visible arch. In this way, the arches we followed are "parents" from the new ones appearing. The step like behavior is obtained again as in figure 10(b), indicating that indeed the velocity mainly increases during merging events.

The same procedure was applied to the simulated velocity field. The corresponding time series is also shown in the inset of figure 11(f). Notice that the first step of the experimental velocity has a value in between two steps of the velocity from the simulation. We associate this with the fact that the arches in experiments have an intermediate size. In experiments, the arches are about 20 length units, while in simulations the arches go from about 10 length units before merging to about 40 length units after merging. Although in simulations the change in velocity from the second to third step is not as abrupt as in experiments, the velocities compare quite well.

REFERENCES

Bruus, H. 2008 *Theoretical microfluidics*. Oxford university press, Oxford.

Scott Jr, T.A. 1946 Refractive index of ethanol–water mixtures and density and refractive index of ethanol–water–ethyl ether mixtures. *J. Phys. Chem.* **50** (5), 406–412.